Science Advances

AAAS

advances.sciencemag.org/cgi/content/full/4/3/eaar3979/DC1

Supplementary Materials for

Stretchable ultrasonic transducer arrays for three-dimensional imaging on complex surfaces

Hongjie Hu, Xuan Zhu, Chonghe Wang, Lin Zhang, Xiaoshi Li, Seunghyun Lee, Zhenlong Huang, Ruimin Chen, Zeyu Chen, Chunfeng Wang, Yue Gu, Yimu Chen, Yusheng Lei, Tianjiao Zhang, NamHeon Kim, Yuxuan Guo, Yue Teng, Wenbo Zhou, Yang Li, Akihiro Nomoto, Simone Sternini, Qifa Zhou, Matt Pharr, Francesco Lanza di Scalea, Sheng Xu

Published 23 March 2018, *Sci. Adv.* **4**, eaar3979 (2018)
DOI: 10.1126/sciadv.aar3979

The PDF file includes:

- section S1. Piezoelectric transducer design using the KLM model
- section S2. SAF imaging and DMAS algorithm
- fig. S1. Testing performance of a commercial rigid probe on curved surfaces.
- fig. S2. Schematic illustration of the device fabrication process.
- fig. S3. Ecoflex thickness as a function of spin coating speed on a glass slide.
- fig. S4. Acoustic damping effects of silicone substrates.
- fig. S5. The vibration mode comparison between PZT and 1-3 composites.
- fig. S6. Pulse-echo response and bandwidth differences of transducers with and without the backing layer (KLM simulation).
- fig. S7. Bottom electrode design.
- fig. S8. Top electrode design.
- fig. S9. Four-layer top electrode fabrication processes.
- fig. S10. Optical images of Cu serpentine interconnections under different laser parameters.
- fig. S11. Laser ablation resolution experiments.
- fig. S12. Photographs of the device seamlessly laminated on different curved surfaces.
- fig. S13. ACF cable bonding.
- fig. S14. Simulation results from the KLM model.
- fig. S15. Dielectric properties of the device.
- fig. S16. The phase angle change during the fabrication process and after repetitive testing.

- fig. S17. Experimental and simulation of a small array under biaxial tensile strain.
- fig. S18. Electric impedances under different bending curvatures.
- fig. S19. The real and imaginary parts of electrical impedance under different levels of bending and stretching.
- fig. S20. Relative resistance changes of Cu serpentine under stretching.
- fig. S21. Instruments for nondestructive evaluation.
- fig. S22. Switch circuit of the entire testing system.
- fig. S23. Reconstructed images based on simulation under flat, concave, and convex surfaces.
- fig. S24. The pulse-echo signal and 2D image of the two defects.
- fig. S25. Polarization conditions.
- fig. S26. The matching circuit of the ultrasound testing system.
- fig. S27. Ultrasound signal filtering.
- fig. S28. Simplified schematics of a transducer element.
- fig. S29. The electrical model of a transducer.
- fig. S30. General diagram showing the transmission line model of a two-port system.
- fig. S31. Schematics showing the basic concept of SAF.
- fig. S32. Block diagrams for the imaging algorithms.
- table S1. Parameters for the 1-3 composite, backing layer, and Ecoflex.
- Reference (*59*)

Other Supplementary Material for this manuscript includes the following:
(available at advances.sciencemag.org/cgi/content/full/4/3/eaar3979/DC1)

- movie S1 (.mp4 format). Simulation of wave field under a planar surface.
- movie S2 (.mp4 format). Simulation of wave field under a concave surface.
- movie S3 (.mp4 format). Simulation of wave field under a convex surface.

section S1. Piezoelectric transducer design using the KLM model

As shown in fig. S28, the designed ultrasonic transducer element is composed of a 1-3 composite, a backing, and an Ecoflex layer: two acoustic ports interact with the back and front surface of the transducer; the Ecoflex layer(s) is desirable as stretchable substrate to sustain active elements and the ‘island-bridge’ structured matrix; a backing layer can be applied to adjust the transducer bandwidth and suppress the ‘ringing effect’ where Z_E is the electrical impedance of the electrical port, and Z_B, Z_C, Z_{Eco}, and Z_T represent the mechanical impedance of the backing layer, active element, Ecoflex layer, and medium, respectively. To facilitate the understanding of the electro-mechanical coupling mechanism, an equivalent circuit model (the KLM model) is implemented for piezoelectric transducer characterization as shown in fig. S29, which allows a transmission line description of the complete transducer design. The piezoelectric element is considered to be a half-wavelength layer, with a central connection to the electrical port via a frequency dependent transformer. The capacitor $C_0 = \frac{\varepsilon^s A}{d}$ is the static dielectric value between the conductive layers of the piezoelectric element within the 1-3 composite, and $C' = -\frac{C_0}{k_t sinc\left(\frac{\omega}{2\omega_0}\right)}$ was a frequency dependent reactance, where ε^s was the electrical permittivity at constant strain, A is the surface area of the transducer element, l was the thickness of the piezoelectric element, ω was the angular frequency, $\omega_0 = \frac{\pi v}{l}$ was the resonance angular frequency of the piezoelectric element, v was the wave velocity in piezoelectric element, and k_t was the electromechanical coupling coefficient. The electro-acoustic transformer has a frequency dependent turns ratio $\psi = k_t\sqrt{\frac{\pi}{\omega_0 C_0 Z_C}}sinc\left(\frac{\omega}{2\omega_0}\right)$, where Z_C was the acoustic impedance of the active element.

Since the transducer only uses the electric port and its front acoustic port to interact with the pulse input and the medium, it can be considered as a two-port system, where the back acoustic port is treated as an internal network. By modeling the transducer as a set of finite transmission lines, the impulse response of the transducer can be estimated by a cascaded two-port system. Considering a general two-port system as a finite transmission line with length *l* shown in fig. S30 (*59*), F_{i1} was the incident wave, F_{i2} is the reflected wave, and F_t is the transmitted wave, where the average potential F and the average current V are represented in Laplace form. The transfer matrix N relates the input and output parameters

$$\begin{pmatrix}\bar{\mathbf{F}}(l)\\ \bar{\mathbf{V}}(l)\end{pmatrix} = N\begin{pmatrix}\bar{\mathbf{F}}(0)\\ \bar{\mathbf{V}}(0)\end{pmatrix} \quad (1)$$

where $N = \begin{pmatrix}n_{11} & n_{12}\\ n_{21} & n_{22}\end{pmatrix}$.

And the input boundary condition of the potential and current can be expressed as

$$\bar{\mathbf{F}}(0) = \bar{\mathbf{F}}_{i1} + \bar{\mathbf{F}}_{i2}, \bar{\mathbf{V}}(0) = \frac{1}{Z_i}(\bar{\mathbf{F}}_{i1} - \bar{\mathbf{F}}_{i2}) \quad (2)$$

where Z_i is the input impedance supply, $i1$ indicates a plane wave traveling in a positive direction and $i2$ in a negative direction. At the end of the transmission line, there is only one plane wave travelling in the positive direction

$$\bar{\mathbf{F}}(l) = \bar{\mathbf{F}}_t, \bar{\mathbf{V}}(l) = \frac{\bar{\mathbf{F}}_t}{Z_T} \tag{3}$$

Substituting (2) and (3) into (1), the transfer function can be expressed as

$$H(p) = \frac{\bar{\mathbf{F}}_t}{\bar{\mathbf{F}}_{i1}} = \frac{2Z_T}{-Z_i Z_T n_{21} + Z_i n_{11} + Z_T n_{22} - n_{21}} \tag{4}$$

where *p* is the Laplace variable. This transfer function allows us to obtain the mechanical form of the sensor response as a function of the excitation. Considering a complete transducer as series of cascaded two-port systems, the transmission and reception transfer function (considering perfect reflection) can be written as

$$H_t(p) = \frac{2Z_T}{-Z_E Z_T N_{t21} + Z_E N_{t11} + Z_T N_{t22} - N_{t21}} \tag{5}$$

$$H_r(p) = \frac{4Z_E Z_T}{(Z_E Z_T N_{t21} - Z_E N_{t11} - Z_T N_{t22} + N_{t21})^2} \tag{6}$$

where $p = i\omega$, Z_E is the electric supply impedance, Z_T is the front load impedance, and N_t is the total transfer matrix. The inverse Fourier Transform is applied on the product of reception transfer function and excitation pulse to estimate the sensor response in the time domain. With the design parameters listed in Table 1, the backing layer can significantly shorten the length of pulse excitation and suppress the ringing effect. Ecoflex serves as the substrate and the front load is a phantom. The estimated sensor response (fig. S14) agrees well with the experimental measurement in Fig. 2B. The discrepancies may have resulted from the uncertainties of the model parameters and/or the mismatch between the model and experimental setup.

table S1. Parameters for the 1-3 composite, backing layer, and Ecoflex.

1-3 composite	
Acoustic Impedance Z_C	20 MR
Relative permittivity ε_{33}	660
PZT Piezoelectric coupling coefficient k_t	0.55
Velocity	3740 m/s
Design frequency	3.5 MHz
Thickness	420 μm
Backing layer	
Acoustic Impedance Z_B	5.92 MR
Ecoflex	
Acoustic Impedance Z_M	1.30 MR
Velocity	948 m/s
Thickness	15 μm

section S2. SAF imaging and DMAS algorithm

Ultrasonic imaging is one of the most popular and successful methods to visualize internal discontinuities in structural or biomedical materials. One widely implemented method is the Phased-Array technique, where multiple transducer elements are excited simultaneously with designed time delays to focus and steer the ultrasonic beam. As an alternative option with simplified hardware requirements, Synthetic Aperture Focus (SAF) for ultrasonic imaging allows a more efficient means of operating the array with excitation of individual elements. A typical SAF approach uses an array of piezoelectric transducers that can act as both transmitters and receivers of ultrasonic waves. The image is constructed by extracting features from the received ultrasonic waveforms that are backpropagated in time to appropriately account for delay due to the relative spatial position of the transmitter, receiver, and focus point. This approach of temporal back propagation, commonly known as Delay-and-Sum (DAS) algorithm, can highlight the coherent wave components due to reflectors and suppress the random noises.

Consider an ultrasonic transducer array with *M* transmitters and *N* receivers, as shown in fig. S31, let the spatial coordinates of each transmitter $i = 1, \dots, M$ be (x_i, y_i) and the spatial coordinates of each receiver $j = 1, \dots, N$ also be (x_j, y_j). A standard DAS algorithm constructs an image $I(x, y)$ by summing at each pixel $P(x, y)$ the amplitudes of the received signals, A_{ij}, appropriately backpropagated, for each combination of transmitter i and receiver j. In the time domain, the backpropagated DAS algorithm is written as

$$I^{DS}(x,y) = \sum_{i=1}^{M}\sum_{j=1}^{N} w_{ij}(x,y)A_{ij}(\tau_{ij,xy}) \tag{7}$$

where w_{ij} are apodization weights, and the backpropagation time, $\tau_{ij,xy}$, corresponds to the travel time of the wave from the transmitter i, to the focus point $P(x,y)$, and back to the receiver j

$$\tau_{ij,xy} = \frac{\sqrt{(x_i-x)^2+(y_i-y)^2}+\sqrt{\left(x_j-x\right)^2+\left(y_j-y\right)^2}}{v} \tag{8}$$

where the denominator is the acoustic wave speed v in the media. The DAS algorithm with uniform unity apodization weights is schematically illustrated as a block diagram in fig. S32A.

An improved SAF technique based on Delay-Multiply-and-Sum (DMAS) algorithm is schematically illustrated as a block diagram in fig. S32B. To reconstruct an image $I(x,y)$ at each pixel $P(x,y)$ with DMAS, considering a linear array of 1×M elements, if the element that transmits does not serve as receiver, with each transmission, $M-1$ ultrasound signals are recorded, so the total number of signals received is $M \cdot (M-1)$. The amplitudes of the received signals, A, are appropriately backpropagated (realigned as in DAS) for each combination of transmitter and receiver. Once all the signals are in phase with regard to pixel

$P(x,y)$, they are combinatorially coupled and multiplied: if the number of received signals is N, then the number of multiplications to be performed is given by all the possible signal pair combinations $\binom{N}{2} = \frac{N^2-N}{2}$. The DMAS beamformed signal is obtained as

$$I^{DMAS}(x,y) = \sum_{i=1}^{N-1} \sum_{j=i+1}^{N} A_i(\tau_{i,xy}) A_j(\tau_{j,xy}) \tag{9}$$

where A_i and A_j are the signals received by the i^th^ and j^th^ transmitter-receiver pairs, respectively, and $\tau_{i,xy}$ and $\tau_{j,xy}$ are the backpropagation times corresponding to the travel times of the wave from the i^th^ and j^th^ transmitter-receiver pairs, respectively, through the focus point $P(x,y)$. To keep the correct scale and same dimensionality without losing its sign, the 'signed' square root of the absolute value of each couple of multiplied signals is placed inside the summation, and the DMAS algorithm can be expressed as

$$I^{DMAS}(x,y) = \sum_{i=1}^{N-1} \sum_{j=i+1}^{N} sign[A_i(\tau_{i,xy}) A_j(\tau_{j,xy})] \sqrt{\left|A_i(\tau_{i,xy}) A_j(\tau_{j,xy})\right|} \tag{10}$$

This process can be interpreted as the auto-correlation function of the receiver aperture and is expected to outperform the conventional DAS framework in terms of improved image lateral resolution and noise rejection, due to the artificially enhanced aperture and coherent component extraction.

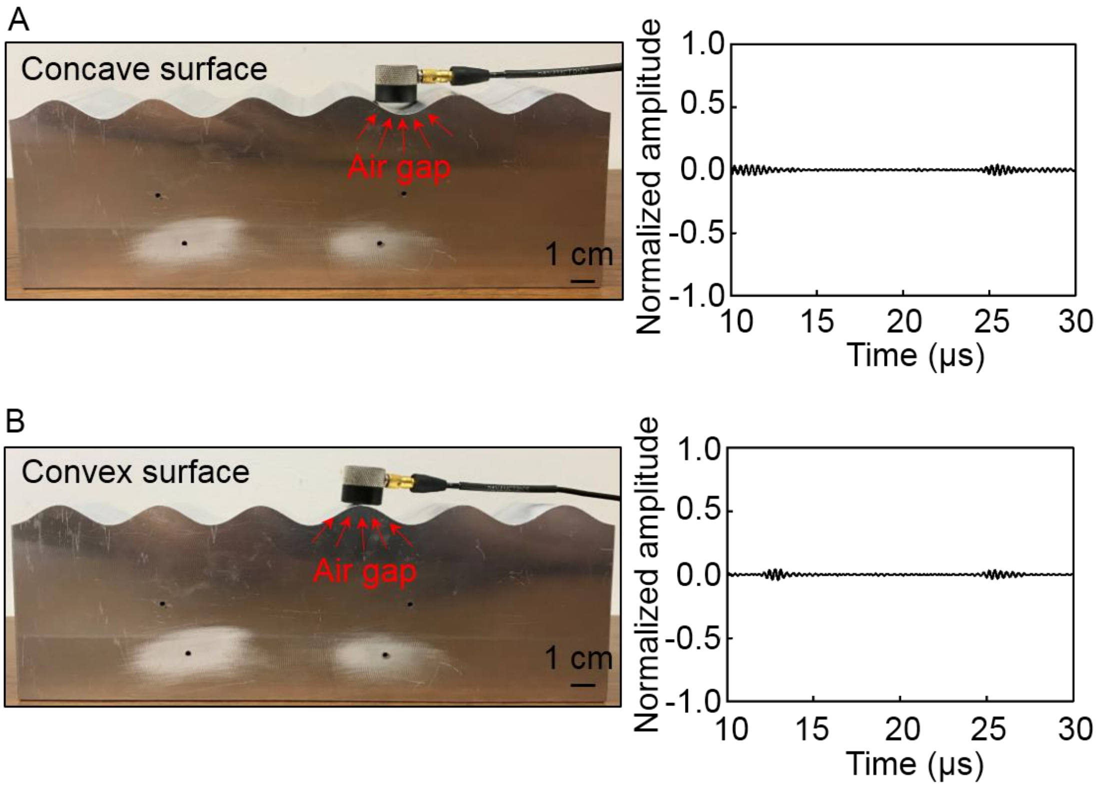

fig. S1. Testing performance of a commercial rigid probe on curved surfaces. A commercial rigid ultrasound probe (V103-RM, Olympus) testing on (A) a concave surface and (B) a convex surface**.** The right columns are the corresponding received signals. The commercial probe cannot seamlessly contact with the curved surfaces. The air gaps between the probe and the subject cause poor acoustic wave propagation. The received signals from concave and convex surfaces, tested by the stretchable device, are in the third column of Figs. 4B and 4C, respectively.

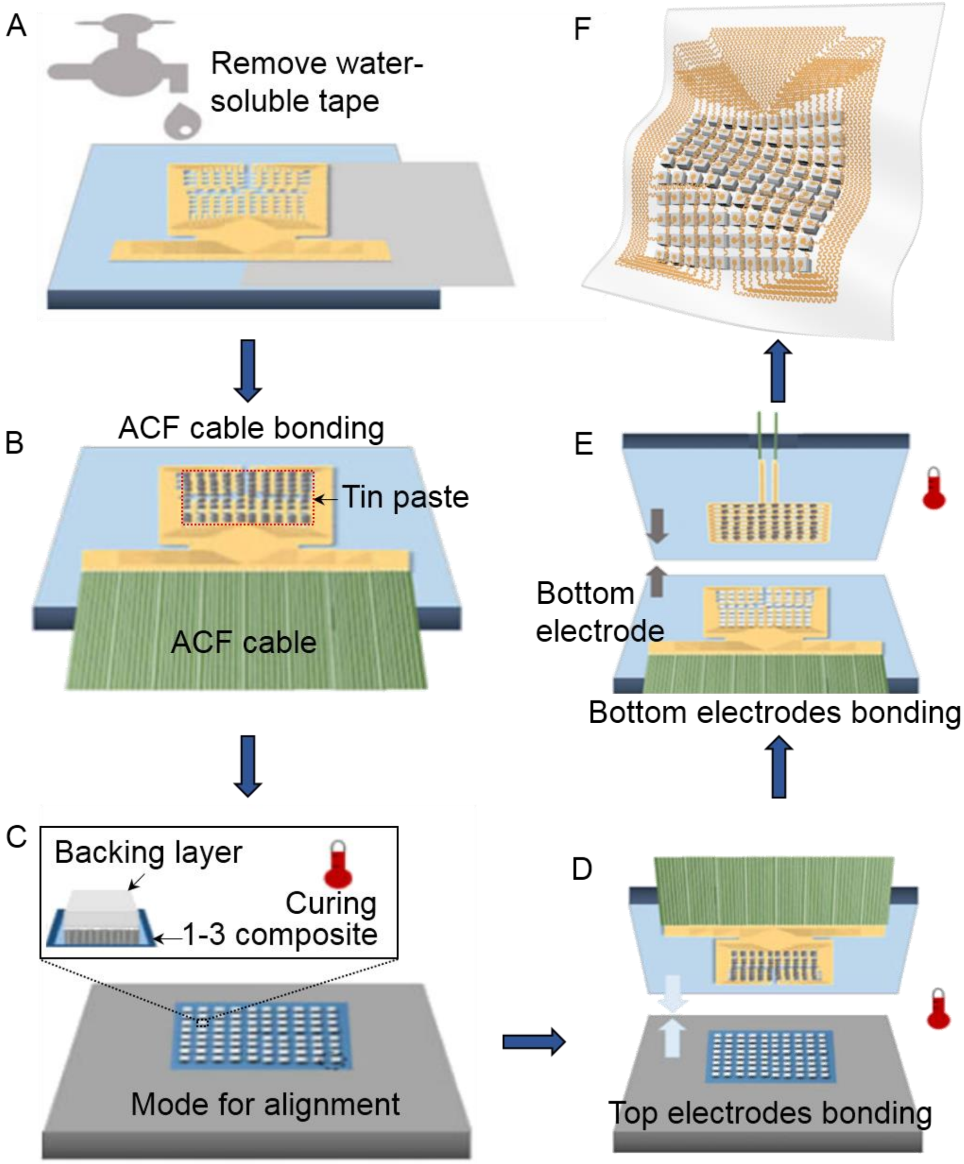

fig. S2. Schematic illustration of the device fabrication process.

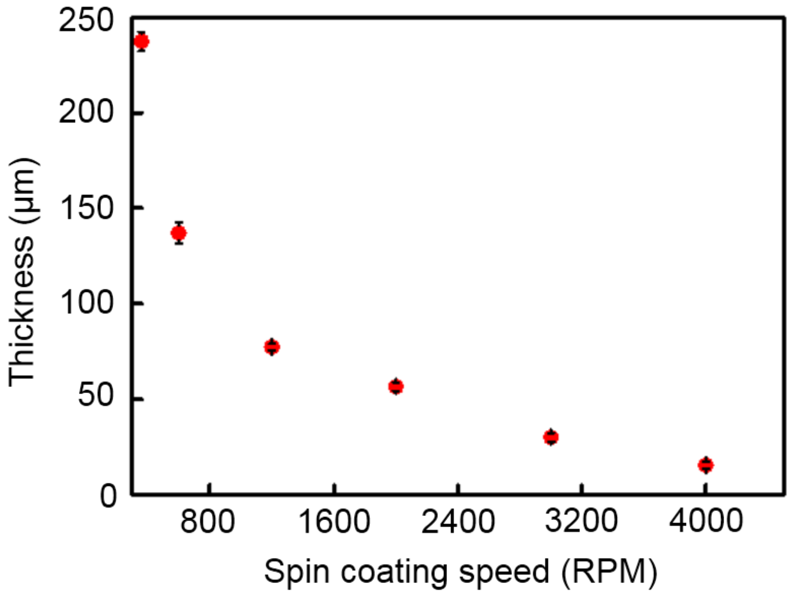

fig. S3. Ecoflex thickness as a function of spin coating speed on a glass slide. Each red data point is averaged from five measurement results. The error bars are indicated in black.

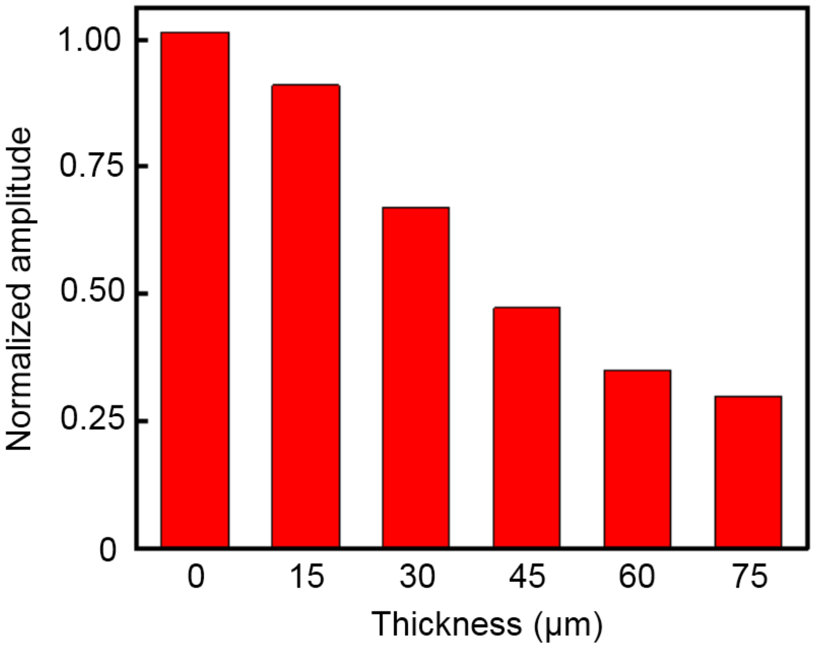

fig. S4. Acoustic damping effects of silicone substrates. Device acoustic emission amplitude is smaller as the thickness of silicone substrate layer at the bottom increases from 0 µm to 15 µm, 30 µm, 45 µm, 60 µm, and 75 µm. However, thin substrates fracture easily. To balance the signal strength and mechanical robustness, 15 µm is used as the bottom layer thickness in this study.

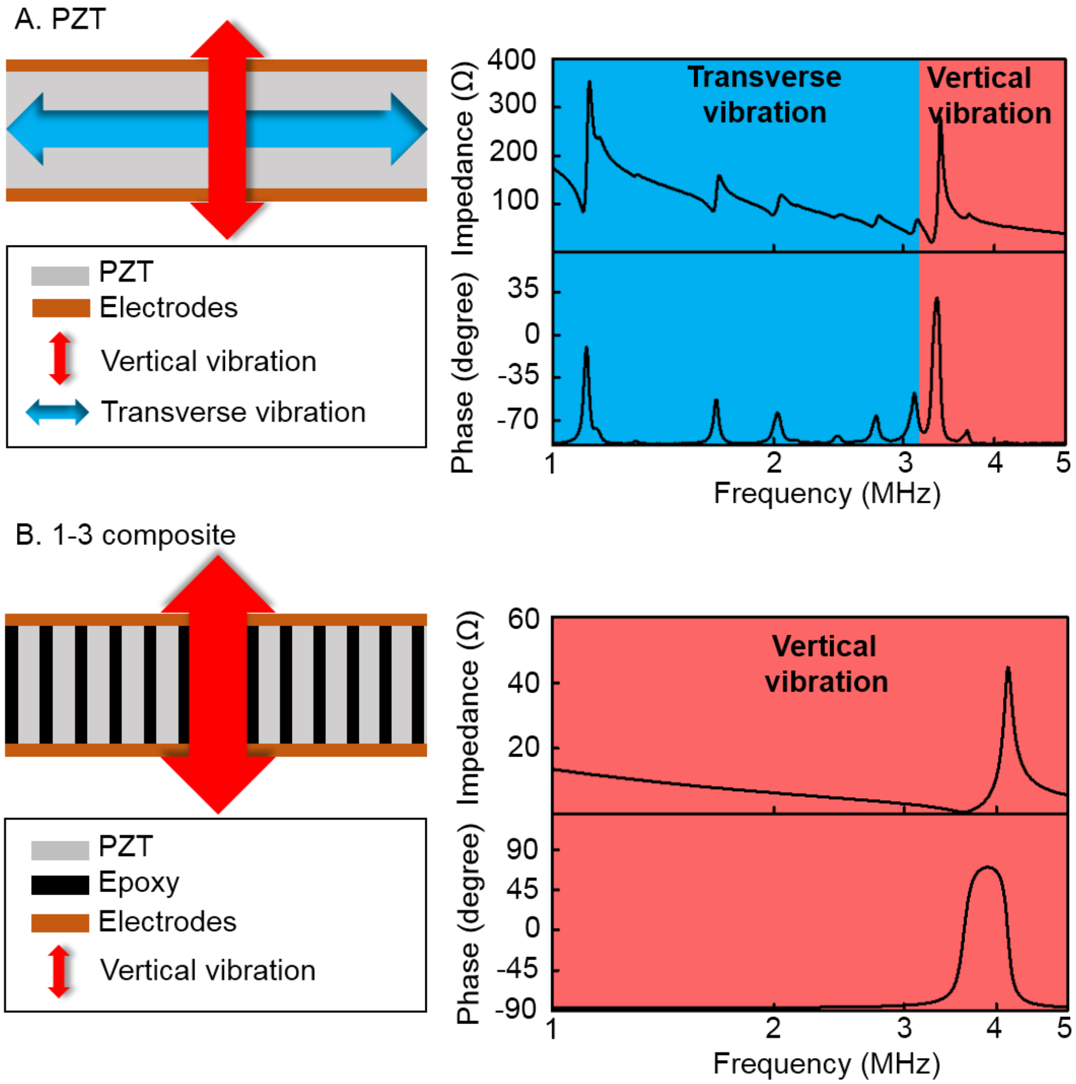

fig. S5. The vibration mode comparison between isotropic PZT and 1-3 composites. Vibration schematics (left) and electrical impedance and phase angle (right) of (A) conventional isotropic PZT and (B) 1-3 composites use in this study. Compared with the isotropic PZT, the epoxy in the 1-3 composites confines the transverse vibration of PZT and thus concentrates the energy on the longitudinal vibration.

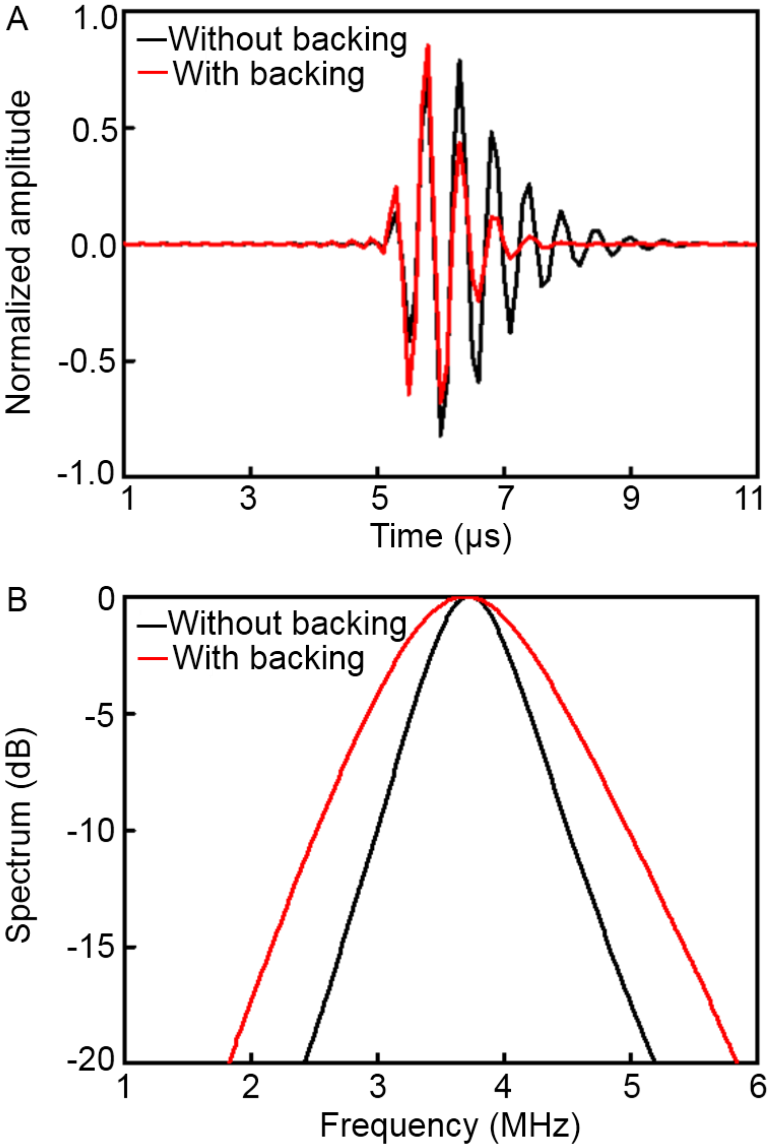

fig. S6. Pulse-echo response and bandwidth differences of transducers with and without the backing layer (KLM simulation). The backing layer dampens the ringing effect, (A) shortens the spatial pulse length, and (B) broadens the bandwidth.

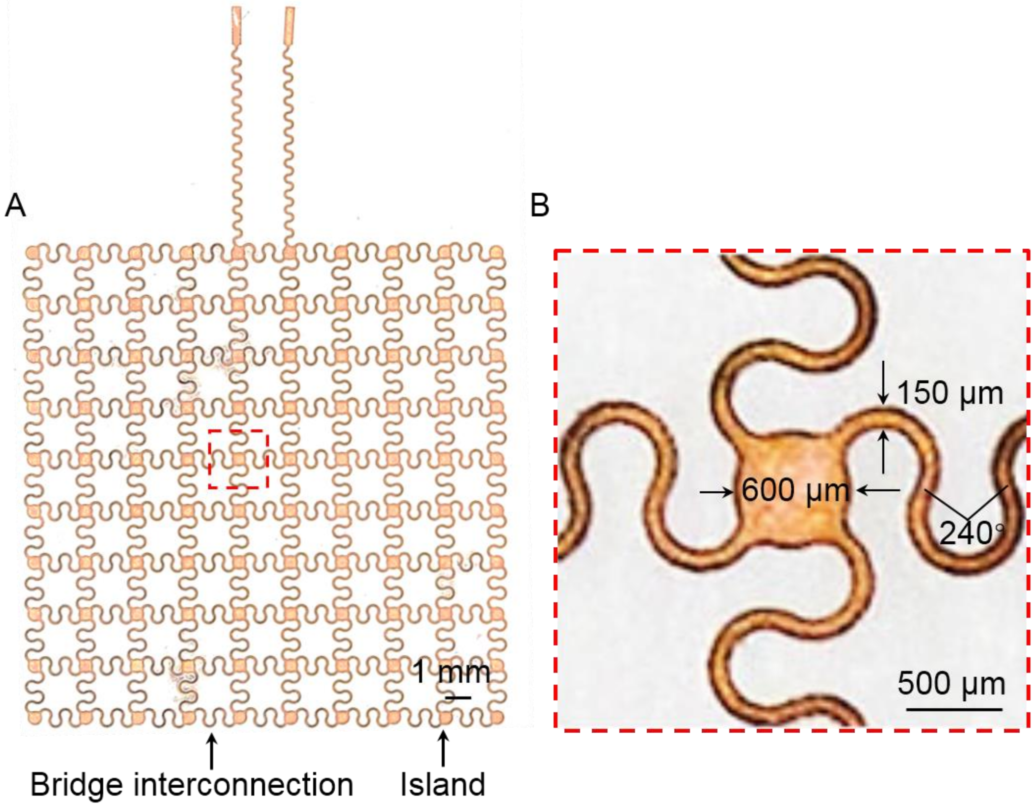

fig. S7. Bottom electrode design. (A) Optical image of the bottom electrode, showing the “island-bridge” structured interconnection. (B) A unit cell of the periodic bottom electrode.

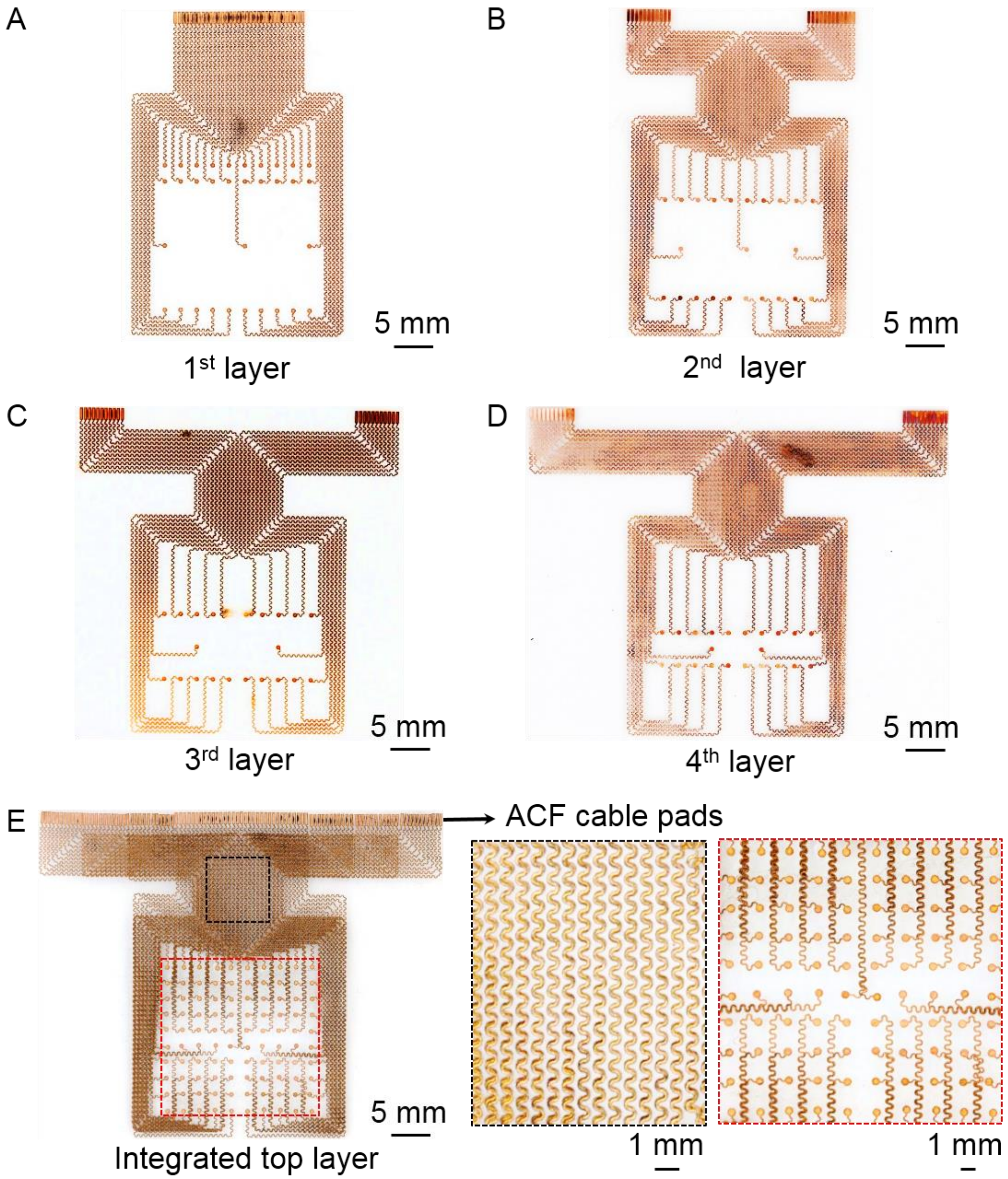

fig. S8. Top electrode design. (A) The 1st, (B) the 2nd, (C) the 3rd, and (D) the 4th layer electrodes. (E) The integrated top electrode, with zoomed-in images showing aligned multilayered serpentine electrodes and contact pads for the transducer elements.

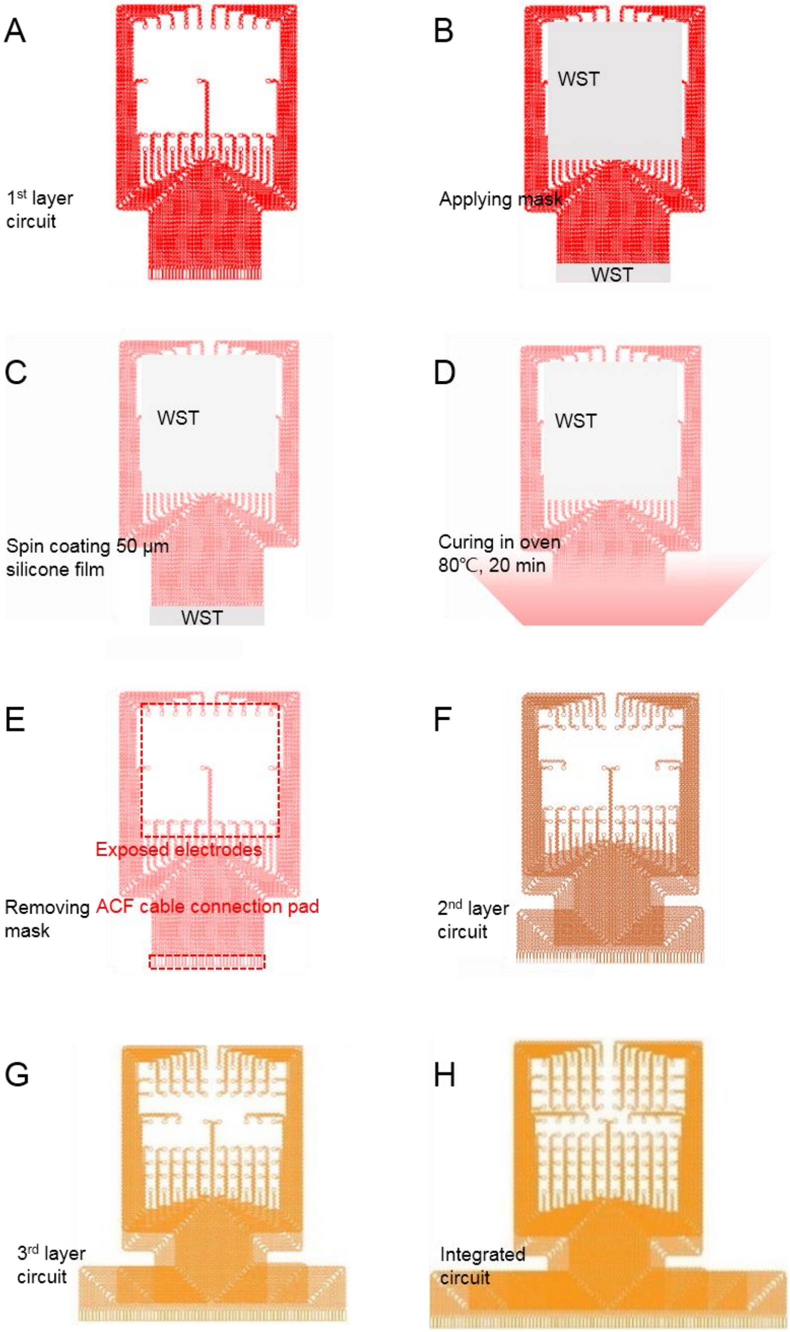

fig. S9. Four-layer top electrode fabrication processes. The electrodes and connection pads are selectively masked by the water soluble tapes. WST: water soluble tape.

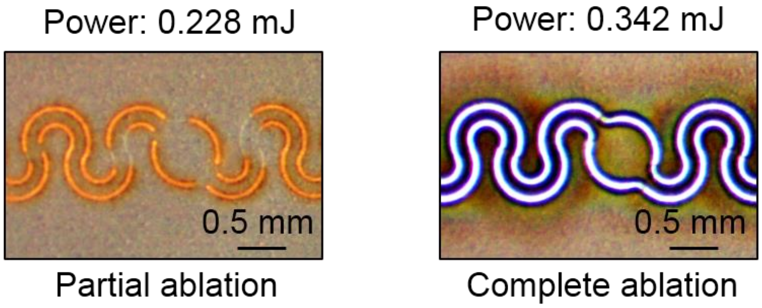

Power: 0.228 mJ

Partial ablation

Power: 0.342 mJ

Complete ablation

Power (%)	**Power (mJ)**	**Frequency (kHz)**	**Speed (mm/s)**	**Pulse width (µs)**
60	0.342	35	300	1
40	0.228	35	300	1

fig. S10. Optical images of Cu serpentine interconnections under different laser parameters. Laser ablation provides a simple, time and cost efficient, and high-yield method for fabricating Cu serpentines.

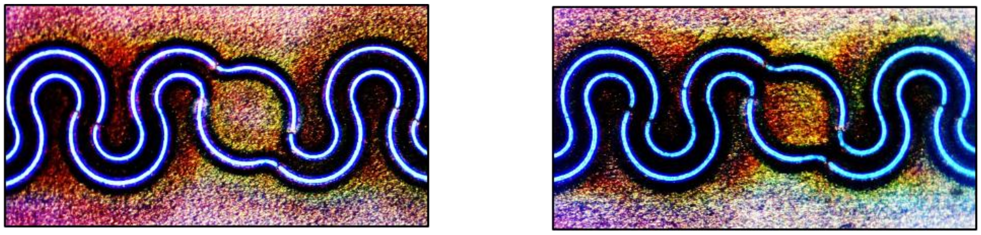

Wire width: 150 µm

Wire width: 120 µm

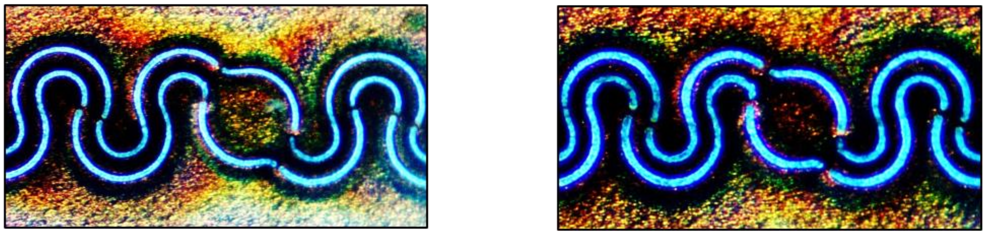

Wire width: 90 µm

Wire width: 60 µm

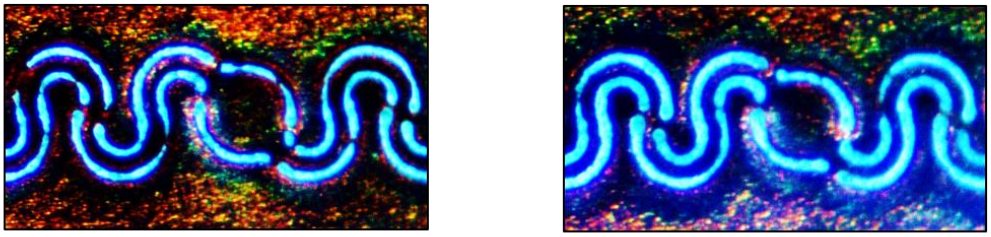

Wire width: 50 µm

Wire width: 40 µm

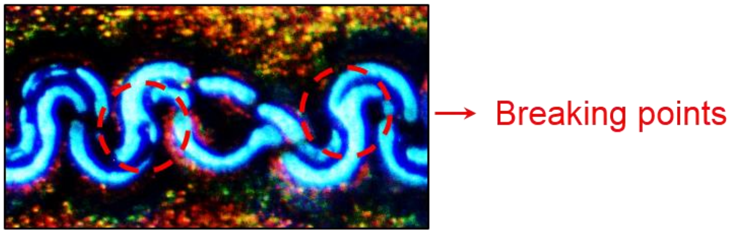

Wire width: 30 µm

fig. S11. Laser ablation resolution experiments. The Cu serpentine wires are designed from 150 µm to 30 µm to verify the laser ablation resolution. Wires with widths of 150 µm to 40 µm remain intact. Discontinuity in the wire starts to show up when the wire width is 30 µm.

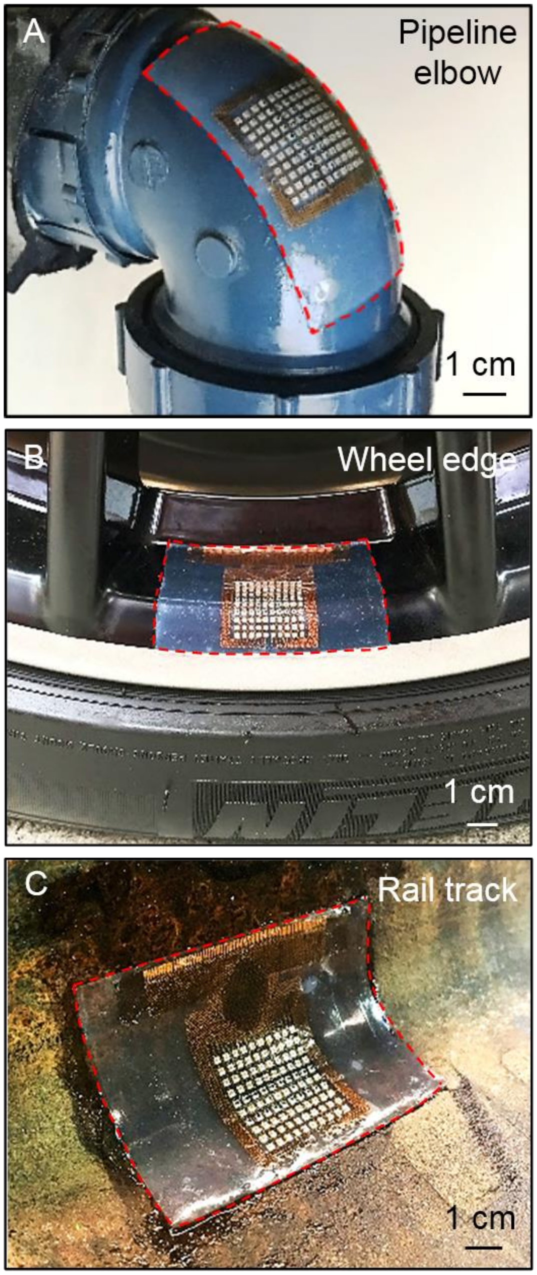

fig. S12. Photographs of the device seamlessly laminated on different curved surfaces. Device conforms to (A) a pipeline elbow, (B) a wheel edge, and (C) a rail track, which show the good mechanical properties of the device.

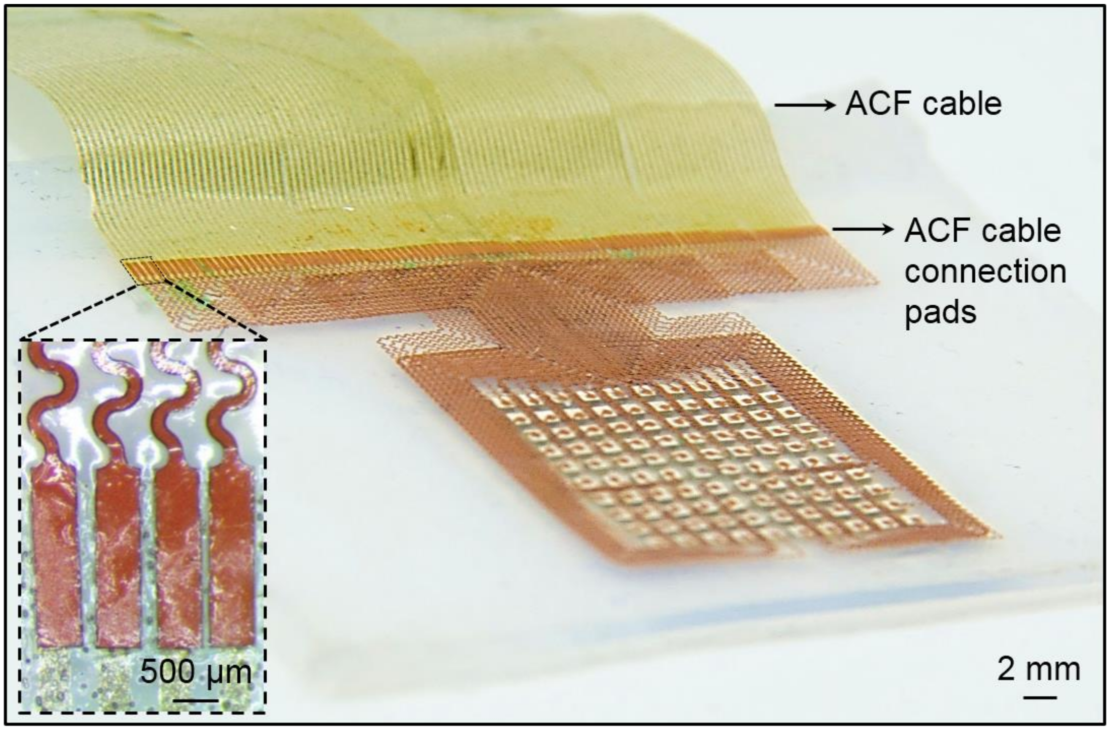

fig. S13. ACF cable bonding. The yield is 100/100 (corresponding to fully functional transducer elements in the array), showing the robustness of the fabrication technology. Inset is the connection interface.

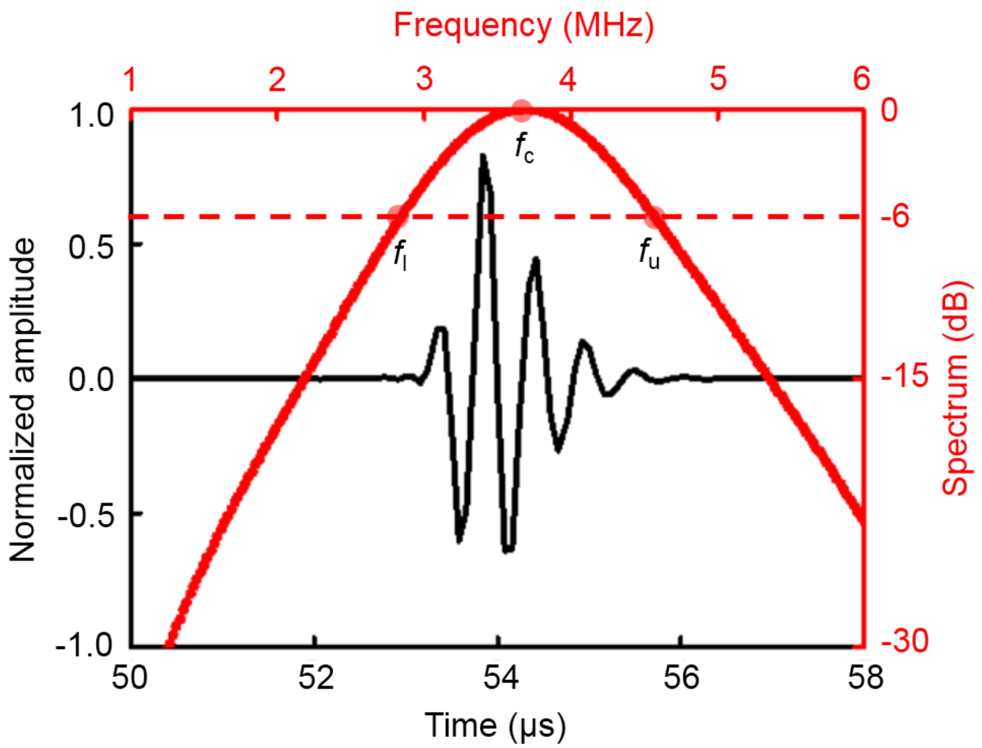

fig. S14. Simulation results from the KLM model. The black curve is the pulse-echo signal response. The red curve is the -6 dB bandwidth (~45.7%). Both match the experiment results (Fig. 2B) very well.

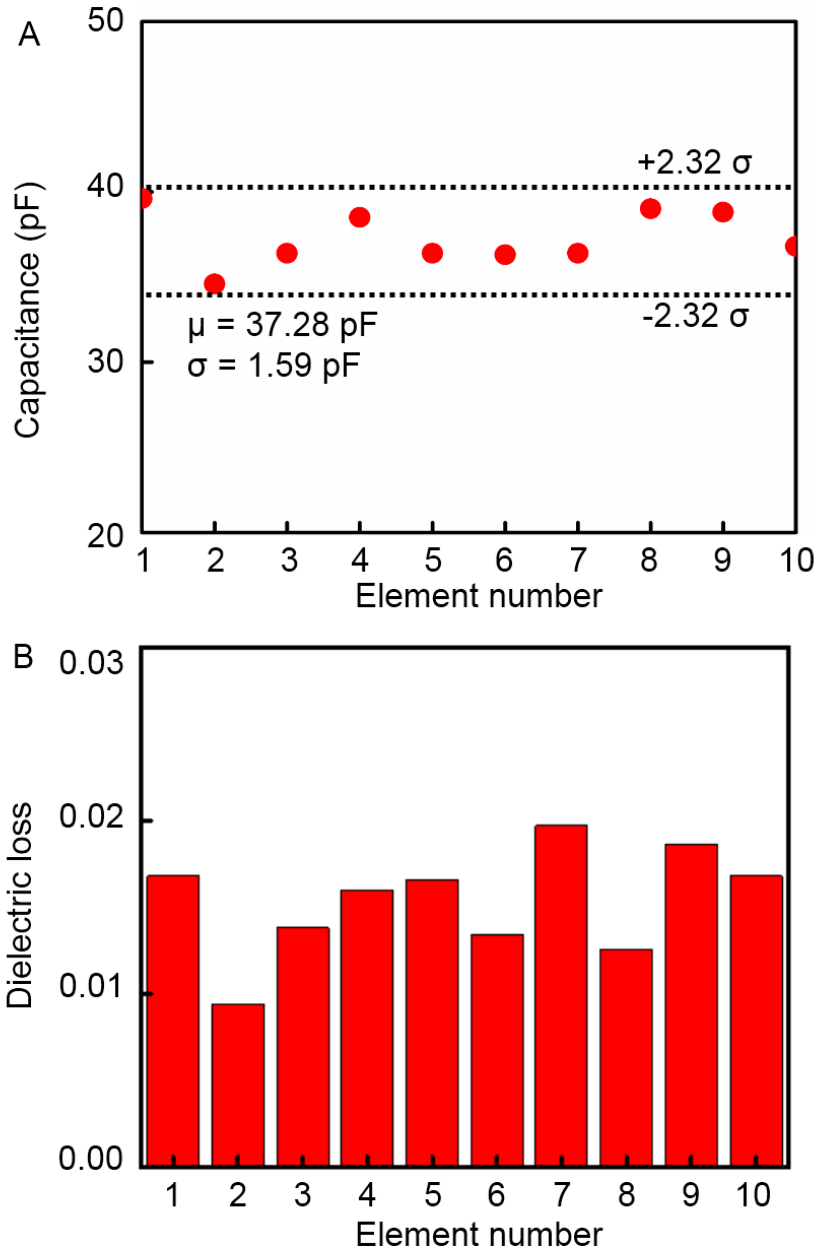

fig. S15. (A) The capacitance and (B) dielectric loss of a 1×10 linear array. μ is the mean value. σ is the standard deviation. These results indicate stable electromechanical coupling performance of the array and the reliable fabrication method.

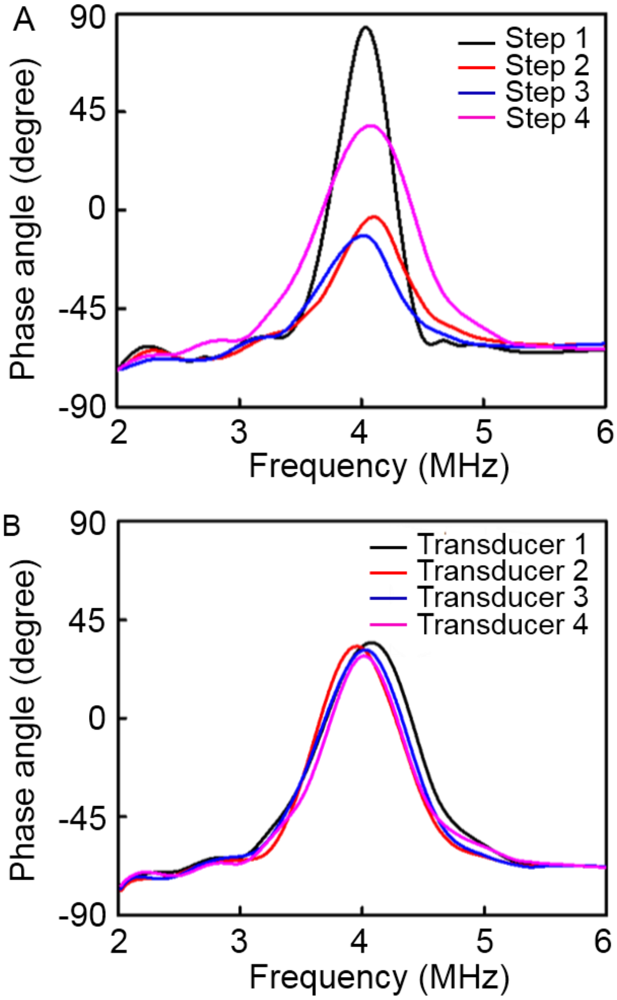

fig. S16. The phase angle change during the fabrication process and after repetitive testing. (A) Processing steps. Step 1 is to dice the 1-3 composite. Step 2 is to bond the backing layer. Step 3 is to bond the top and bottom Cu electrodes. Step 4 is to encapsulate and pole the 1-3 composite under 52.38 kV/cm for 15 minutes. (B) Repetitive testing. After processing, four transducer elements have similar phase angles, showing the reproducibility and robustness of our process.

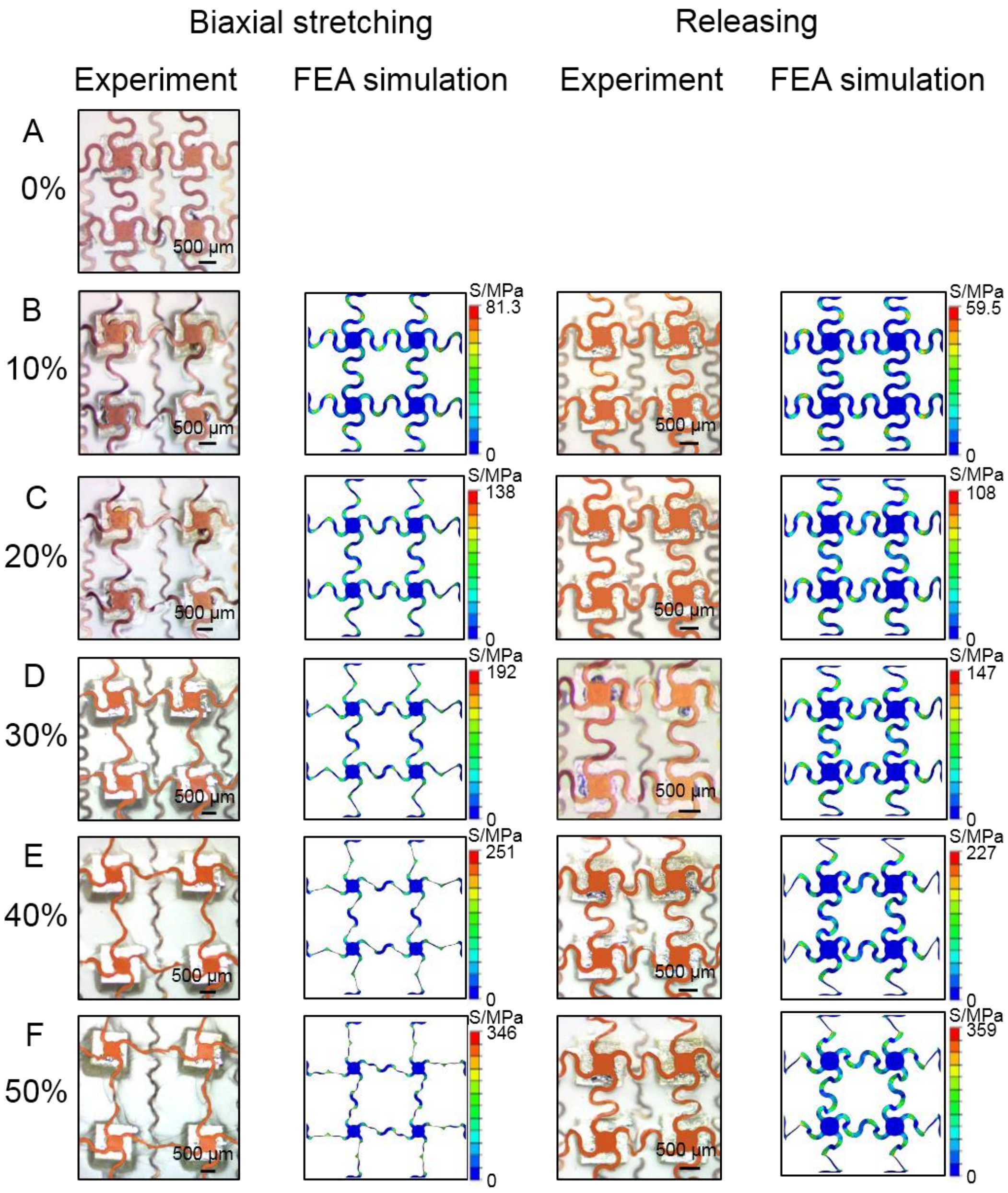

fig. S17. Experimental and simulation results of a small array under biaxial tensile strain. Good agreement exists between the experiments and simulations. The results show an elastic stretchability of ~30%.

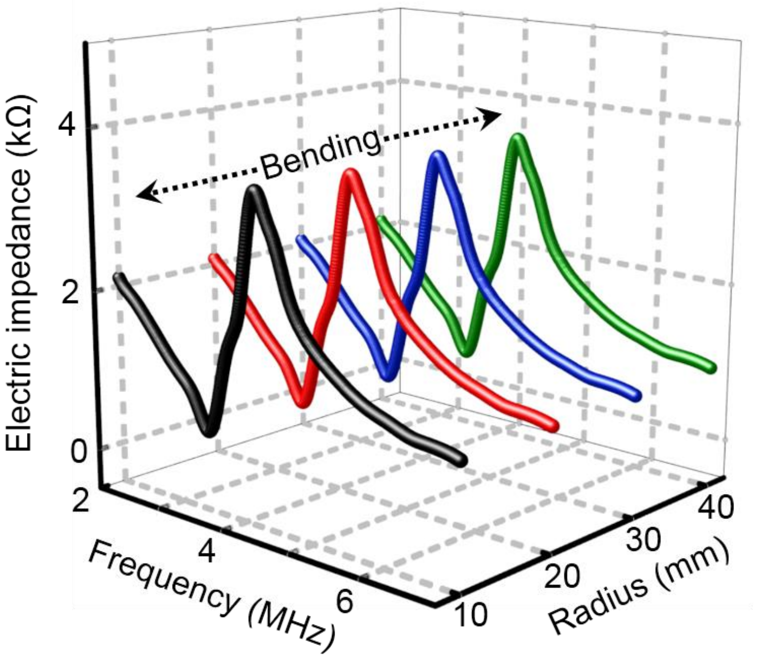

fig. S18. Electric impedances under different bending curvatures. These experimental results show that bending produces minimal effects on the performance of the device.

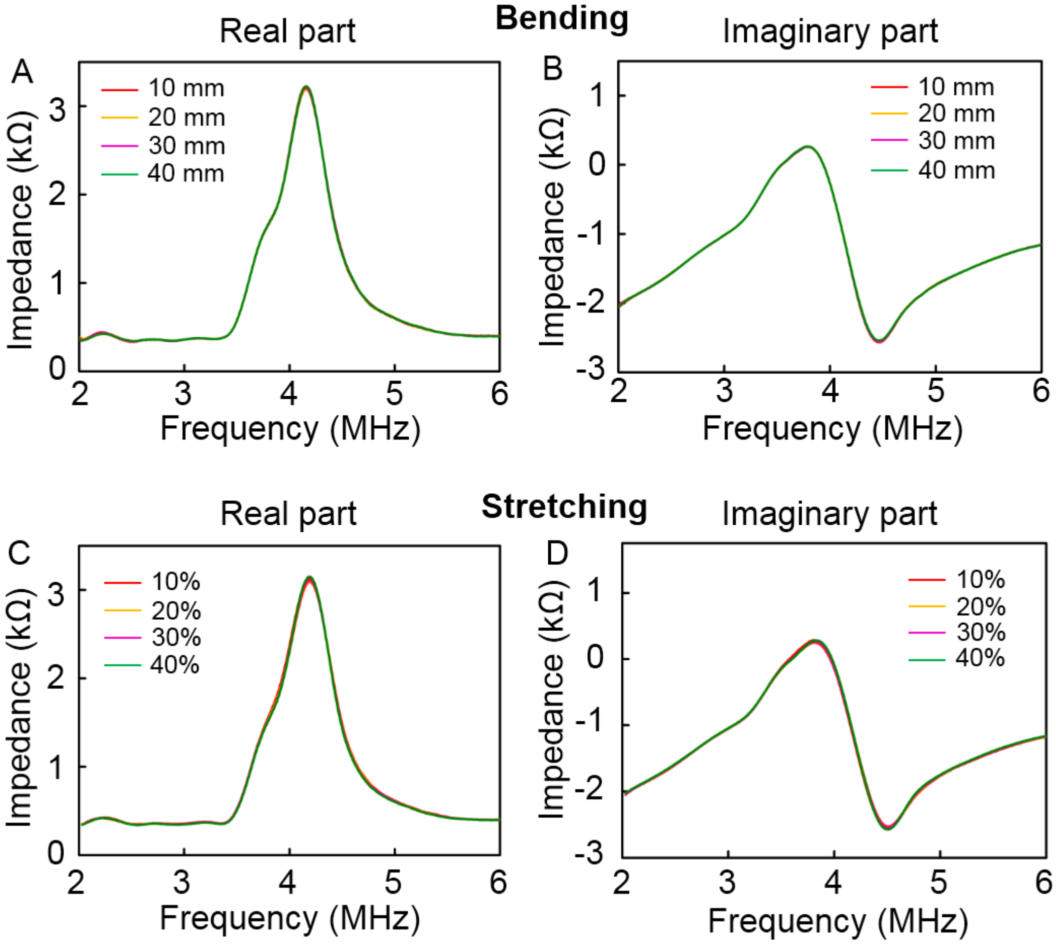

fig. S19. The real and imaginary parts of electrical impedance under different levels of bending and stretching. The (A) real and (B) imaginary parts of electrical impedance under bending to different radii of curvature. The (C) real and (D) imaginary parts of electrical impedance under different levels of tensile strain. The mechanical deformations have minimal effects on the performance of the device.

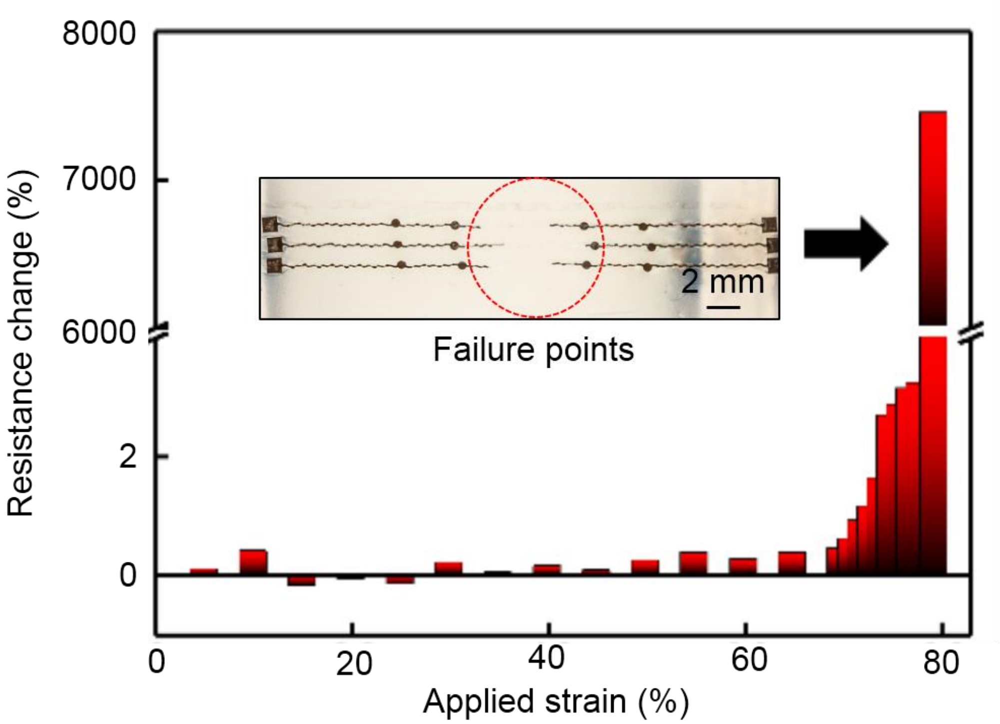

fig. S20. Relative resistance changes of Cu serpentine under stretching. The resistance of a serpentine remains relatively constant until approaching the failure point, which shows that stretching has minimal effect on the conductivity of the interconnects prior to fracture.

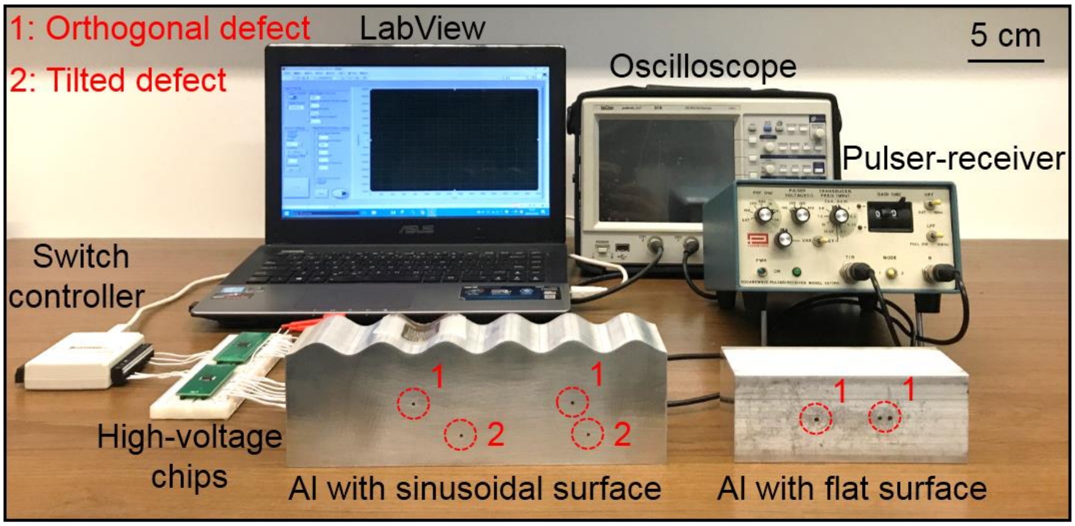

fig. S21. Instruments for NDE testing. The key components and features are all highlighted in the image.

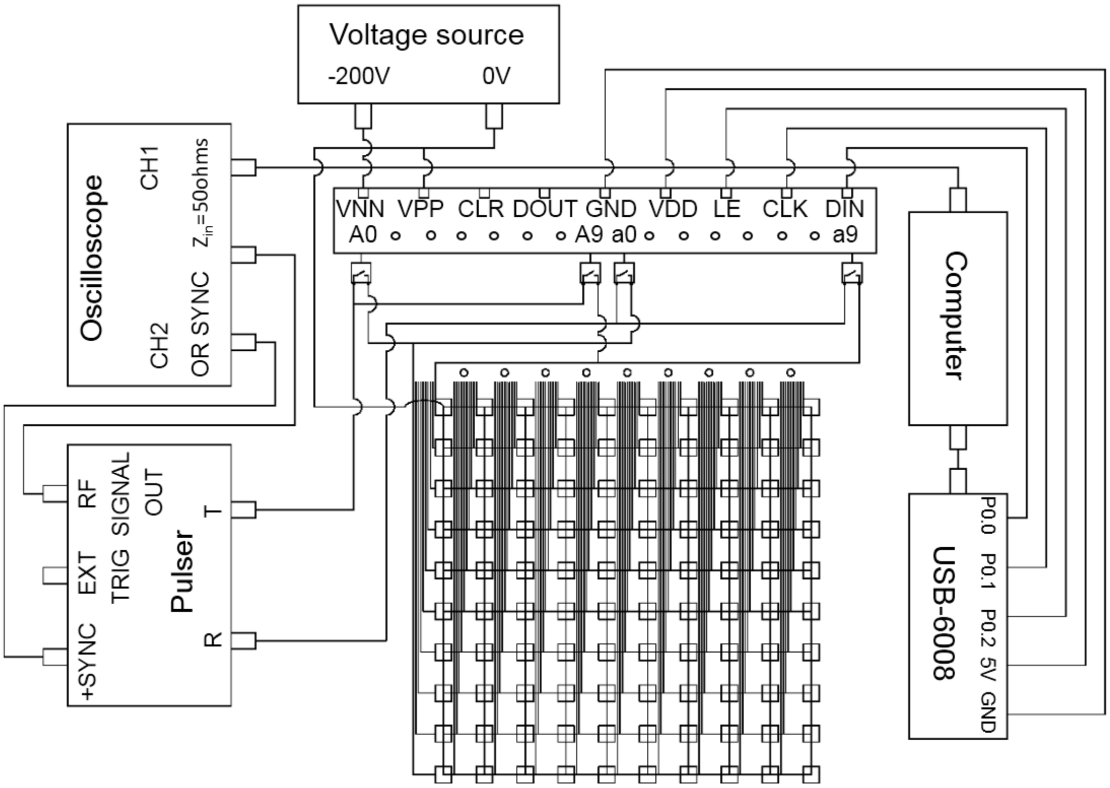

fig. S22. Switch circuit of the entire testing system. This setup allows the device to automatically transmit and receive ultrasound signals.

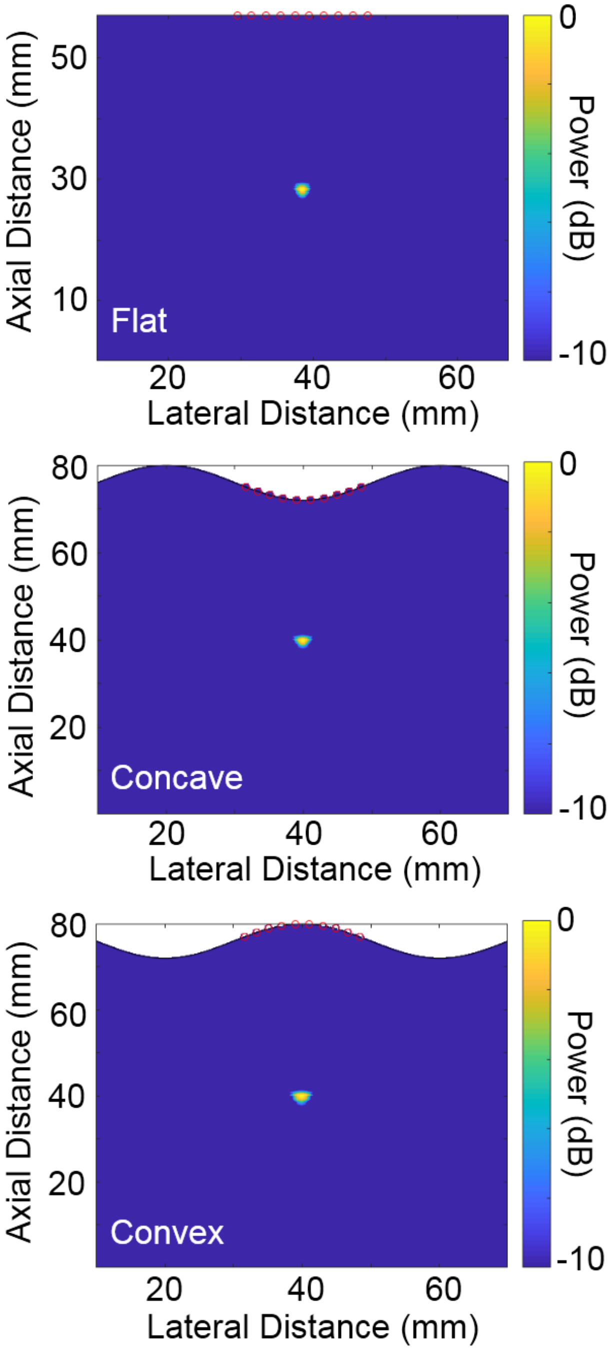

fig. S23. Reconstructed images based on simulation under flat, concave, and convex surfaces. These results match well with the design in Figs. 4A to 4C, respectively.

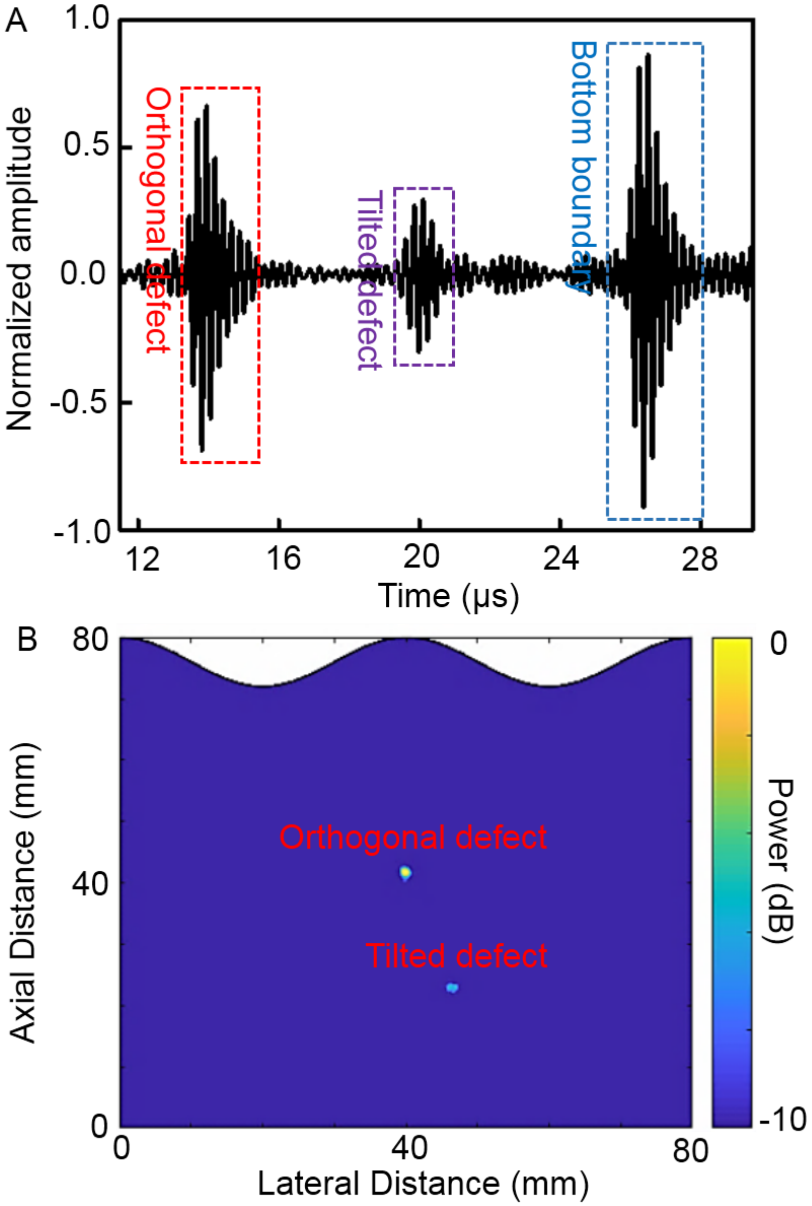

fig. S24. The pulse-echo signal and 2D image of the two defects. (A) The clear pulse-echo signals of the two defects and the bottom boundary acquired by a linear array. (B) The reconstructed 2D image of the two defects. The shadowing effect causes a smaller intensity of the tilted defect compared with the orthogonal defect. This image shows the excellent performance of our device and the advantages of the DMAS imaging algorithm used in this study.

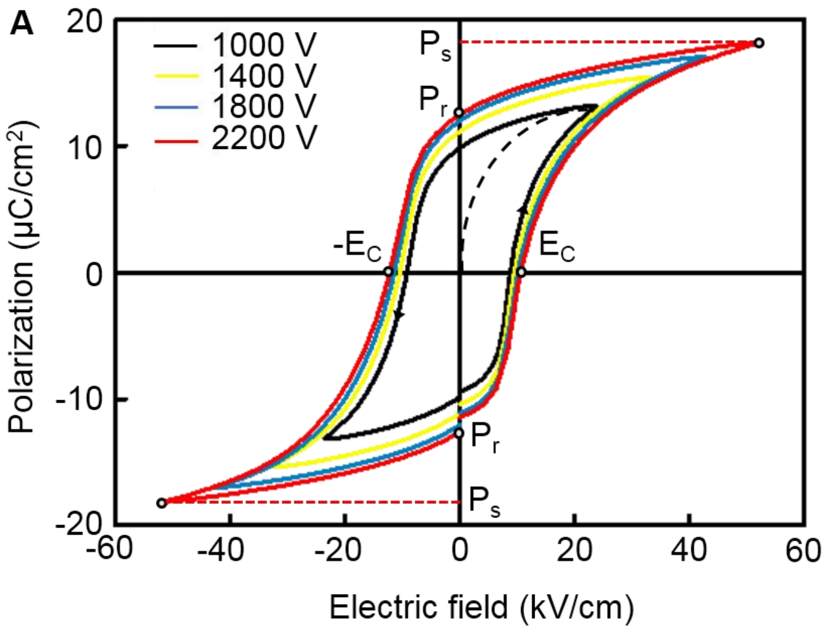

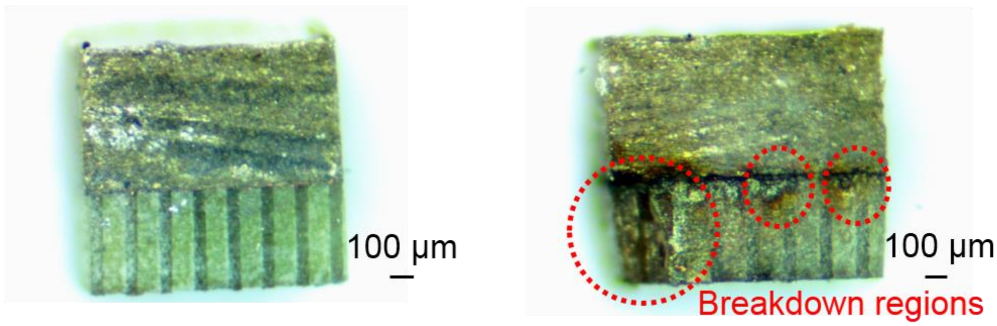
B. Normal polarization at 52.38 kV/cm

C. Breakdown above 52.38 kV/cm

fig. S25. Polarization conditions. (A) Polarization hysteresis loops under different poling voltages. Cross-section of a transducer element (B) after polarization at 52.38 kV/cm in a silicone medium and (C) after breakdown at above 52.38 kV/cm.

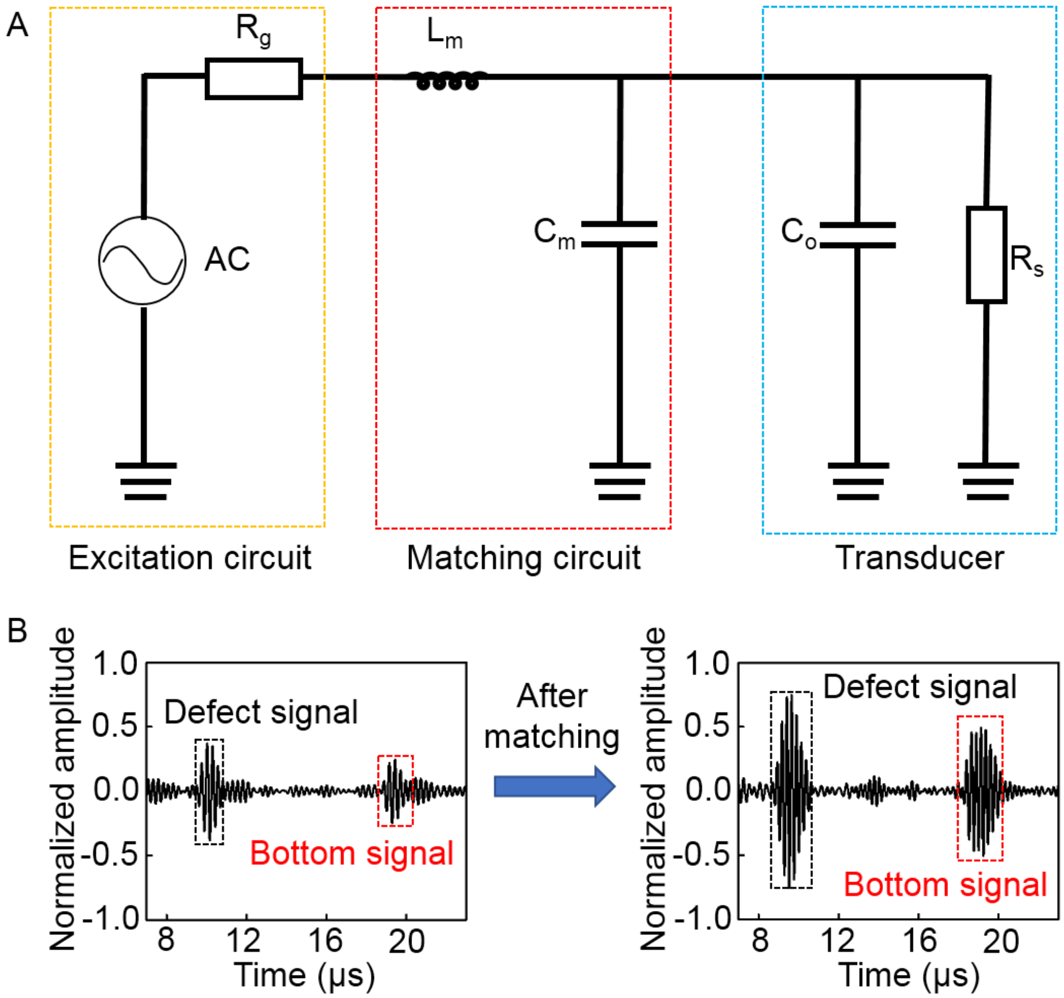

fig. S26. The matching circuit of the ultrasound testing system. (A) The matching circuit design. (B) Ultrasound echo signal before and after implementing the matching circuit in the testing system. The matching circuit will minimize the power reflection during the excitation of the acoustic transmitter, improving the power transmission efficiency, thereby optimizing the SNR.

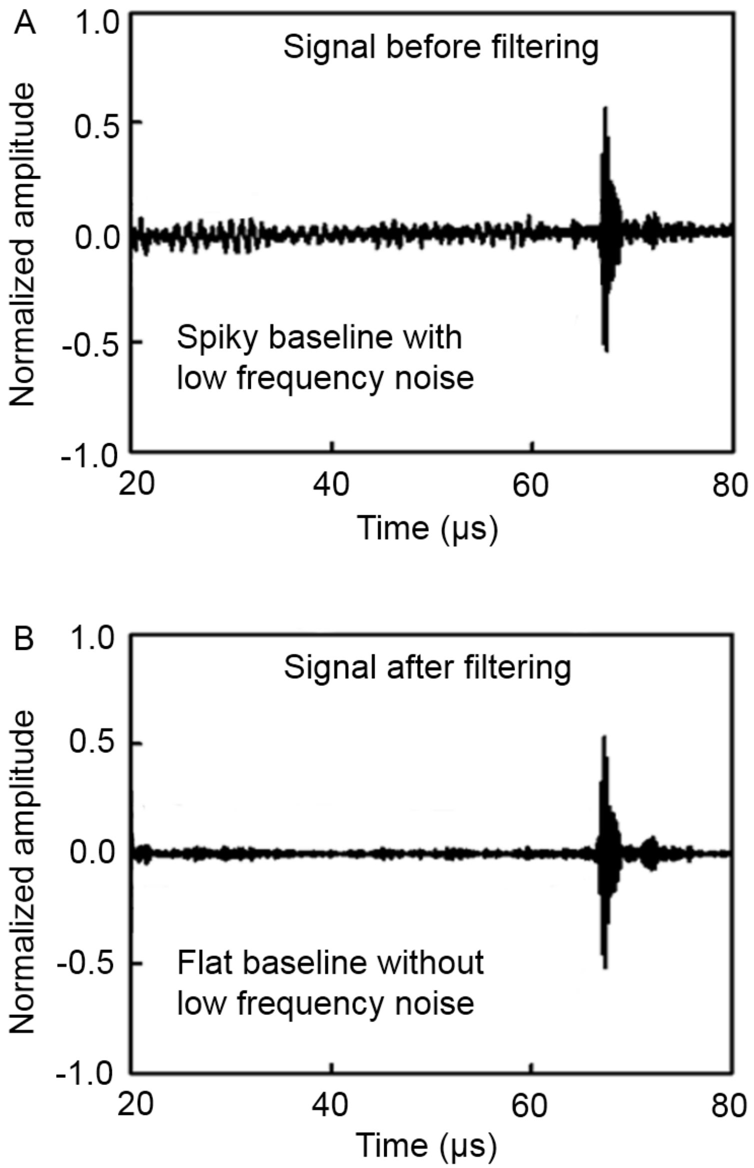

fig. S27. The comparison of ultrasonic performance (A) before and (B) after filtering. Signal filtering with wavelet transform can effectively remove low frequency noise to increase the SNR.

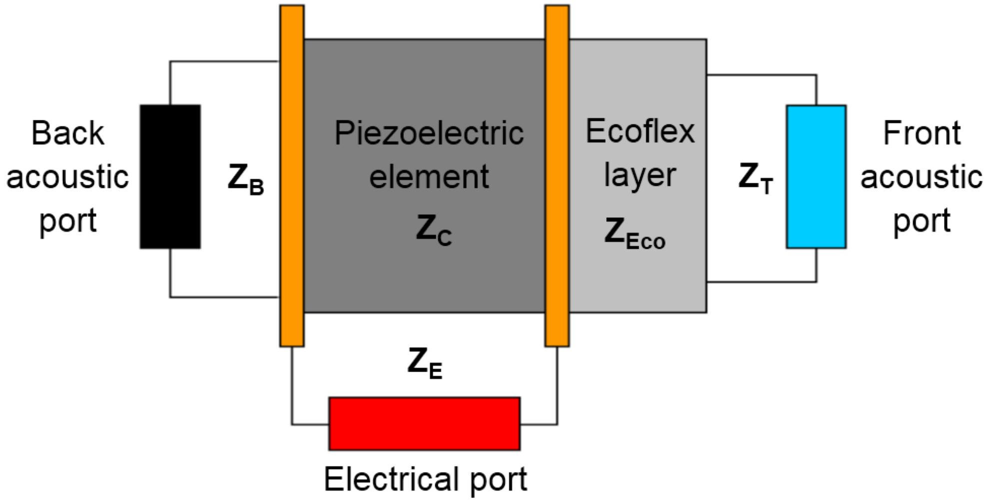

fig. S28. Simplified schematics of a transducer element. The piezoelectric element is covered by conductive layers and connected to the electrical port, showing the typical ultrasound transducer design including both the electrical and mechanical ports.

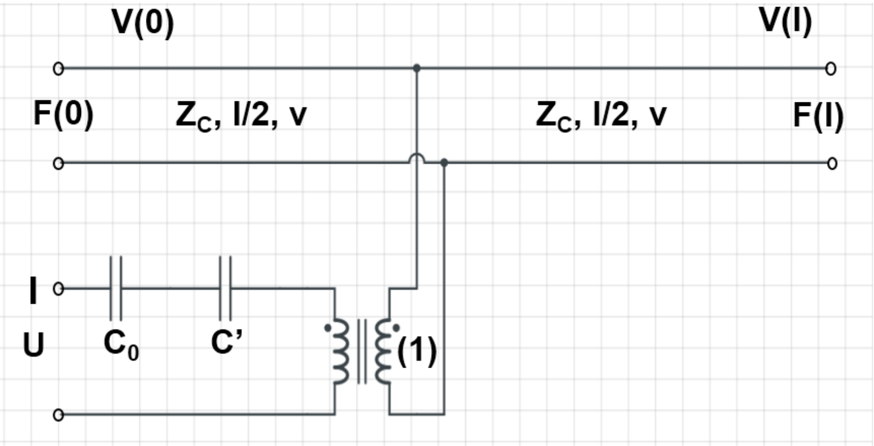

fig. S29. The electrical model of a transducer. It shows the equivalent circuit for a piezoelectric transducer using the KLM model.

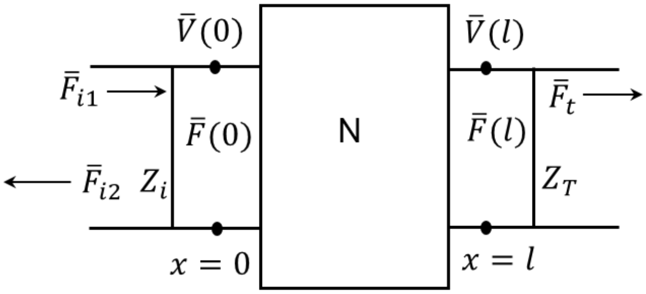

fig. S30. General diagram showing the transmission line model of a two-port system.

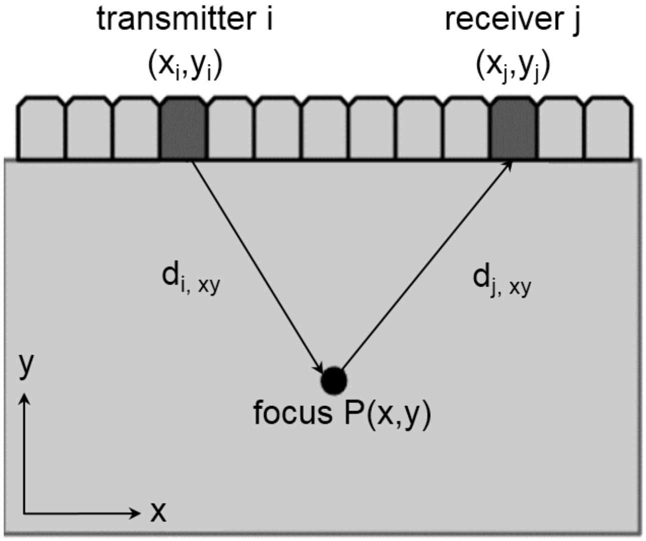

fig. S31. Schematics showing the basic concept of the synthetic aperture focus.

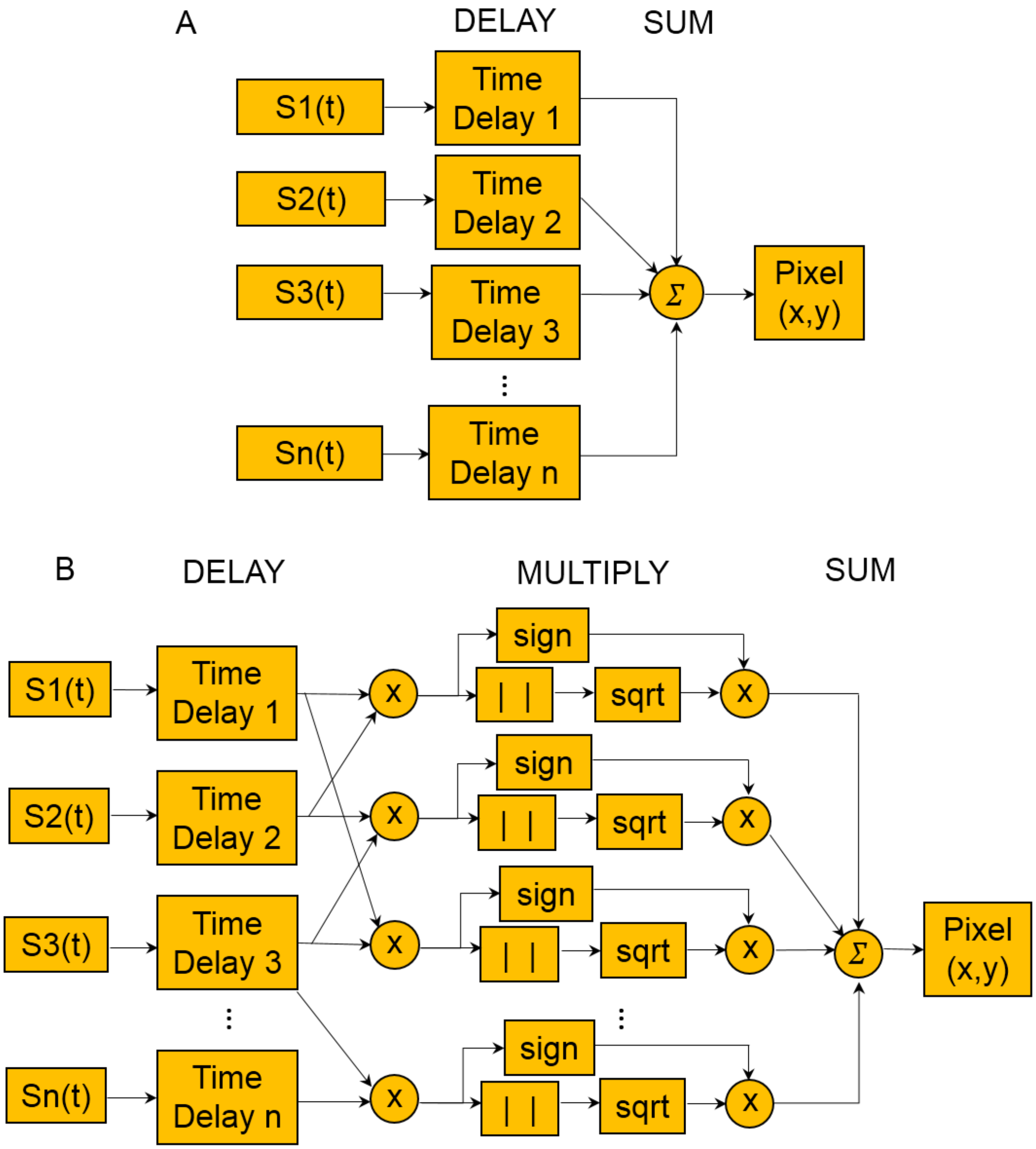

fig. S32. Block diagrams for (A) DAS and (B) DMAS. Compared with DAS, DMAS used in this study takes advantage of the combinatorial correlation measure among all signal pairs, which improves the SNR significantly, making images more accurate and artifact-free.